www.sciencemag.org/cgi/content/full/333/6043/755/DC1

Supporting Online Material for

High-Speed Atomic Force Microscopy Reveals Rotary Catalysis of Rotorless F_1-ATPase

Takayuki Uchihashi, Ryota Iino, Toshio Ando,* Hiroyuki Noji*

*To whom correspondence should be addressed. E-mail: hnoji@appchem.t.u-tokyo.ac.jp (H.N.); tando@staff.kanazawa-u.ac.jp (T.A.)

Published 5 August 2011, *Science* **333**, 755 (2011)
DOI: 10.1126/science.1205510

This PDF file includes:

Materials and Methods
Figs. S1 to S12
Table S1
References (*26–28*)

Other Supporting Online Material for this manuscript includes the following:
(available at www.sciencemag.org/cgi/content/full/333/6043/755/DC1)

Movies S1 to S8

Supporting Online Materials

High-speed atomic force microscopy reveals rotary catalysis of rotor-less F_1-ATPase

Takayuki Uchihashi, Ryota Iino, Toshio Ando, Hiroyuki Noji

MATERIALS AND METHODS

Purification of $\alpha_3\beta_3$ subcomplex and measurement of ATP hydrolysis rate
Fixation of $\alpha_3\beta_3$ subcomplex onto substrate for AFM observation
High-speed AFM apparatus
AFM imaging and image processing
Correlation analysis
Measurement of cumulated number of CCO shifts
Measurement of cumulated rotational angle
Calculation of the degree of underestimation of unidirectionality
Simulation of AFM image

SUPPORTING FIGURES S1 TO S12

S1: Purification and ATPase activity of $\alpha_3\beta_3$ subcomplex
S2: Comparison of raw, temporally filtered, and spatially filtered AFM images
S3: Wide-area AFM images of $\alpha_3\beta_3$ subcomplex without nucleotide and in 2 mM ATP
S4: Three dimensional illustrations of the crystal structure and AFM image in nucleotide-free condition.
S5: Experimental and simulated AFM images of the N-terminal side of $\alpha_3\beta_3$ subcomplex
S6: Tight correlation between two types of conformational changes in β observed in ATP
S7: Reference AFM images and ROIs used in the correlation analysis of β conformations observed in ATP
S8: Correlation coefficient analysis of three βs in $\alpha_3\beta_3$ subcomplex observed in nucleotide-free condition
S9: Correlation coefficient analysis of three βs in $\alpha_3\beta_3$ subcomplex observed in AMPPNP
S10: Distributions of the number of successive shifts of "CCO" state in clockwise and counterclockwise directions

S11: Histograms of dwell times for the O and C states in various [ATP]

S12: Loss of a single subunit stops rotary propagation of conformational changes

SUPPORTING TABLE S1

S1: Fraction of molecules showing conformational changes in various nucleotide conditions.

SUPPORTING ONLINE MOVIES S1 TO S8

Movie S1: AFM movie of the C-terminal side of $\alpha_3\beta_3$ without nucleotide. Scan area, 18 × 15 nm^2; frame rate, 10 fps.

Movie S2: AFM movie of the N-terminal side of $\alpha_3\beta_3$ without nucleotide. Scan area, 17 × 11 nm^2; frame rate, 10 fps.

Movie S3: AFM movie of the C-terminal side of $\alpha_3\beta_3$ in 2 μM ATP. Scan area, 17 × 13 nm^2; frame rate, 12.5 fps.

Movie S4: AFM movie of the C-terminal side of $\alpha_3\beta_3$ in 3 μM ATP. Scan area, 18 × 14 nm^2; frame rate, 12.5 fps.

Movie S5: AFM movie of the C-terminal side of $\alpha_3\beta_3$ in 4 μM ATP. Scan area, 17 × 11 nm^2; frame rate, 12.5 fps.

Movie S6: AFM movie of the C-terminal side of $\alpha_3\beta_3$ in 2 μM ATP. Scan area, 21 × 14 nm^2; frame rate, 12.5 fps. The pixel with the highest (brightest) position in each image is indicated by the blue circle. The center used for calculating the rotational angle is indicated by the cross mark.

Movie S7: AFM movie of the C-terminal side of $\alpha_3\beta_3$ in 2 μM ATP. Scan area, 21 × 14 nm^2; frame rate, 12.5 fps. At 16 s, one β subunit was lost.

Movie S8: AFM movie of the C-terminal side of $\alpha_3\beta_3$ in 2 μM ATP. Scan area, 25 × 14 nm^2; frame rate, 12.5 fps. At 9 s, one α subunit was lost.

MATERIALS AND METHODS

Purification of $\alpha_3\beta_3$ subcomplex and measurement of ATP hydrolysis rate

The $\alpha(His_6$ at N-terminus/C193S$)_3\beta(His_3$-Lys_7 at N-terminus$)_3$ subcomplex of the F_1-ATPase from thermophilic *Bacillus sp.* PS3 was expressed in *E. coli*, and purified using Ni^{2+}-NTA affinity chromatography and size exclusion chromatography as described previously for purification of the $\alpha_3\beta_3\gamma$ subcomplex (*26*) (Fig. S1). The nucleotide-free $\alpha_3\beta_3$ subcomplex was stable and stored at room temperature before use. The ATP hydrolysis rate was measured with an ATP regenerating system using a UV-visible spectrophotometer (VP-550, Jasco). Various concentrations of ATP were added to the assay mixture (10 mM Tris-HCl (pH 8.0), 2 mM $MgCl_2$, 250 mM KCl, 2.5 mM phosphoenolpyruvate, 0.1 mg/ml pyruvate kinase, 0.1 mg/ml lactate dehydrogenase, and 0.2 mM NADH) at 0 s, followed by the addition of $\alpha_3\beta_3$ (final 30 nM) at 200 s. The NADH absorbance at 340 nm was monitored and the initial rate of ATP hydrolysis was calculated from the initial slope (for 10 s after the addition of $\alpha_3\beta_3$) of the change in [NADH] using a molecular extinction coefficient of 6,220. Measurements were carried out at 24–25 °C (Fig. S1).

Fixation of $\alpha_3\beta_3$ subcomplex onto substrate for AFM observation

To fix the $\alpha_3\beta_3$ subcomplex onto a mica substrate, we first treated the mica surface with 3-aminopropyl-triethoxysilane (0.05–0.1%) for 3 min and washed the surface with pure water. The mica was then treated with glutaraldehyde (0.1–0.25%) for 3 min and carefully washed with buffer A (10 mM HEPES-NaOH (pH 7.4), 10 mM KCl, 5 mM $MgSO_4$). A droplet containing the $\alpha_3\beta_3$ subcomplex (1–10 nM) was deposited on the surface for 5 min, which was then washed with buffer B (10 mM Tris-HCl (pH 8.0), 2 mM $MgCl_2$). The sample stage was mounted on the AFM head and immersed in buffer B with or without ATP or AMPPNP. AFM imaging showed that the $\alpha_3\beta_3$ subcomplex was strongly adsorbed on the mica surface by chemical cross-linking between the primary amine on the aminosilane-modified mica and the ε-amines of the lysine residues in the N-terminus of the β subunit. Judging from the observed images and height of the molecules (~9 nm), almost all molecules appeared to be adsorbed on the mica at either the C- or N-terminal side. Most (~70%) of the adsorbed molecules had the C-terminal side facing upward, whereas the rest had the N-terminal side facing upward. On bare and untreated mica surfaces, all molecules rapidly diffused on the surface and could not be imaged clearly.

High-speed AFM apparatus

We used a home-built high-speed AFM apparatus (*17*, *18*). The cantilevers (Olympus) were 6–7 μm long, 2 μm wide, and 90 nm thick. Their spring constant was 0.1–0.2 N/m, and their resonant frequency and quality factor in an aqueous solution were 0.7–1 MHz and ~2, respectively. For AFM imaging, the free oscillation amplitude was ~1 nm and the set-point amplitude was around 90% of the free oscillation amplitude. The tapping force estimated was less than 30 pN (*27*). An amorphous carbon tip was grown on the original tip by electron beam deposition (*28*). The tip length was adjusted to ~1 μm. The tip was sharpened by plasma etching under argon gas (tip apex, ~4 nm in radius).

AFM imaging and image processing

All AFM observations were performed at room temperature (24–26 °C). We usually used a scan area of ~45 × ~22 nm^2 with (100–150) × (50–75) pixels. The AFM images were captured at frame rates of 10–12.5 fps. After taking images, we tracked a target molecule using two-dimensional (2D) correlation analysis to compensate for the slow drift of the sample stage position in the x- and y-directions. A 3 × 3 pixel-average filter was applied to each tracked image to reduce noise. For the AFM images obtained under nucleotide-free and AMPPNP conditions in which the conformational change does not occur, frame averaging was applied before the pixel averaging (Fig. S2). The AFM images were displayed first with black-to-white color scale and then the color scale was nonlinearly assigned to the height level to highlight the top-surface structure (Fig. S4).

Correlation analysis

To determine the time evolution of the conformational state of each β subunit, we calculated a 2D correlation coefficient for its image in the following way. As shown in Fig. S7, for each β we arbitrarily chose a reference frame and a region of interest (ROI) so that the ROI in the reference frame fully contained an open-state β subunit. The 2D correlation coefficient defined below was calculated frame-by-frame for each ROI. For images obtained in AMPPNP, we chose a closed- or open-state β subunit as the reference. The 2D correlation coefficient is defined as,

$$r = \frac{\sum_m \sum_n (H_{mn} - \bar{H})(R_{mn} - \bar{R})}{\sqrt{(\sum_m \sum_n (H_{mn} - \bar{H})^2)(\sum_m \sum_n (R_{mn} - \bar{R})^2)}}$$

Here, H_{mn} and R_{mn} are heights at pixel point (m, n) in a to-be-analyzed ROI and a reference ROI of the reference frame, respectively. $\bar{H}$ and $\bar{R}$ are mean values of the

height matrices H and R, respectively.

Measurement of cumulated number of CCO shifts

As mentioned in the main text, the most populated conformational state was the CCO state, in which one β subunit is in the open (O) state and the other two are in the closed (C) state. The other conformational states (COO, CCC, OOO) were much less frequent and therefore considered to be unusual conformations. To reveal unidirectional propagation of the conformational states, we defined the cumulated number of the CCO shifts (N_{CCO}) as follows. When the CCO state first appears in successive AFM images, N_{CCO} is set to be 1. Then, when the CCO state shifts counterclockwise, N_{CCO} is increased by 1. In contrast, when the CCO state shifts clockwise, N_{CCO} is reduced by 1. Here, unusual states are ignored and therefore do not affect N_{CCO}. This counting was carried out for all consecutive frames.

Measurement of cumulated rotational angle

The open-state β had a higher protrusion than that of the closed-state β (Fig. 1). We obtained the pixel position that has the highest intensity in each frame (P), and tracked such positions in consecutive images (see inset of Fig. 2B). The averaged position of the tracked highest-intensity positions was defined as the center (O). The cumulated rotational angle of the $\overrightarrow{OP}$ relative to the vector $\overrightarrow{OP}$ in the first frame was then calculated.

Calculation of the degree of underestimation of unidirectionality

In the experiment shown in Fig. 2 and 3, the frame capture time (t) was 80 ms and the time constant (τ) of the open state at 2 μM ATP was 0.66 s (Fig. S11) irrespective of counterclockwise or clockwise shift. Assuming a Poisson process, the probability ($P(N)$) that the shifts occur N-times within the frame capture time can be calculated by following equation.

$$P(N) = (1/N!) \times (t/\tau)^N \times \exp(-t/\tau)$$

Thus, the probability of single clockwise shift within the frame capture time is $(1/1)\times(0.08/0.66)\times\exp(-0.08/0.66) = 0.107$, and that of two consecutive counterclockwise shifts is $(1/2)\times(0.08/0.66)^2\times\exp(-0.08/0.66) = 0.0065$. Using these values, fraction of the two consecutive counterclockwise shifts included in the apparent single clockwise shift was estimated to be $\{0.0065/(0.0065+0.107)\} \times 100 = 5.7\%$.

Simulation of AFM image

We used software (SPM simulator, Advanced Algorithm Systems Co., Tokyo, Japan) to simulate AFM images of the $\alpha_3\beta_3$ attached to a substrate surface at either the C- or N-terminal side. The simulation was carried out with a simple hard-sphere model. The cantilever tip was modeled as a circular cone (apex angle, 10°) with a small sphere (radius, 0.5–2 nm) at the apex. Crystal structures of the nucleotide-free $\alpha_3\beta_3$ subcomplex (PDB code, 1SKY) and nucleotide-bound $\alpha_3\beta_3\gamma$ subcomplex (PDB code: 1BMF) were used as the samples. For the latter case, the γ subunit was removed from the crystal structure. Each atom in the protein was modeled as a hard sphere with a corresponding van der Wars radius. We simulated AFM images using various radii for the tip-apex sphere and found that a radius of 0.5 nm produced the images most similar to the actual AFM images. The simulated images were processed by a low-pass filter with a cut-off wavelength of 2 nm, because the spatial resolution of the AFM image was approximately 2 nm judging from the 2D Fourier transformation of actual AFM images.

LEGENDS FOR SUPPORTING FIGURES

Fig. S1. Purification and ATPase activity of $\alpha_3\beta_3$ subcomplex. (A) SDS-PAGE of purified $\alpha_3\beta_3$ and $\alpha_3\beta_3\gamma$ subcomplexes. (B) ATP hydrolysis rate of $\alpha_3\beta_3$ as a function of ATP concentration. The rate obeyed Michaelis-Menten kinetics (solid line), yielding a Michaelis constant (K_m) of 12 μM and a maximum velocity (V_{max}) of 12 s^{-1}.

Fig. S2. Comparison of raw, temporally filtered, and spatially filtered AFM images. (A), (B), and (C) correspond to the raw, frame-averaged (22 frames), and 3 × 3 pixel-averaged images obtained without nucleotide, respectively. Scan range, 16 nm × 16 nm. Pixel numbers, 46 pixels × 46 pixels. (D) and (E) correspond to the raw and pixel-averaged images in 2 μM ATP. Scan range, 14 nm × 14 nm. Pixel numbers, 32 pixels × 32 pixels.

Fig. S3. Wide-area AFM images of $\alpha_3\beta_3$ subcomplex without nucleotide and in 2 mM ATP. Frame rate, 1 fps. Scale bar, 20 nm. (A) An AFM image without nucleotide. In this image, all molecules show a pseudo-six-fold symmetric ring shape in which three βs in the ring are in the open state. (B) An AFM image in 2 mM ATP. Because the rate of conformational change was high in this ATP concentration as compared with the

frame rate of observation, all molecules showed a triangle shape in which βs in the ring are almost in the closed state (66% of a frame capture time) during scanning. These results indicate that almost all of $\alpha_3\beta_3$ molecules behave in the same way and show different conformations depending on the presence and absence of ATP.

Fig. S4. Three dimensional illustrations of the crystal structure and AFM image in nucleotide-free condition. The α and β subunits of the crystal structure are colored in cyan and pink, respectively. The C-terminal DELSEED motif of β corresponding to the high protruding portions is highlighted in red. The color scale to display the AFM image is not linearly set for the height level. This is because the height of $\alpha_3\beta_3$ is about 9 nm but the height variation at the top-most surface is less than 1 nm. To highlight the top-most structure contained in the AFM image, the complete dark scale is used for the height regions from the bottom to 80% of the highest position. Above this threshold, a linear brightness scale is used.

Fig. S5. Experimental and simulated AFM images of the N-terminal side of $\alpha_3\beta_3$ subcomplex (Online movie S2). (A) An AFM image experimentally obtained without nucleotide. (B) N-terminal side of the atomic structure of $\alpha_3\beta_3$ subcomplex (PDB code: 1SKY). The α and β subunits are colored in cyan and pink, respectively. (C) Simulated AFM image constructed from the atomic structure (PDB code: 1SKY).

Fig. S6. Tight correlation between two types of conformational changes in β observed in ATP; different heights of protrusion ("H," high; "L," low) and open (O)/closed (C) conformations of the distal region. The higher protrusion is mostly accompanied by the open conformation, whereas the lower protrusion is mostly accompanied by the closed conformation.

Fig. S7. Reference AFM images and regions of interest (ROIs) used in the correlation coefficient analysis of β conformations observed in ATP (results shown in Fig. 2). The transparent boxes show ROIs. The image of β in each ROI appears to be in the open state.

Fig. S8. Correlation coefficient analysis of three βs in $\alpha_3\beta_3$ subcomplex observed in nucleotide-free condition. (A) AFM image of $\alpha_3\beta_3$. (B) Reference images and ROIs used in the correlation analysis. For each β, an arbitrary image was chosen as the reference image. (C) Correlation coefficient distributions for the three βs. (D) Time

courses of correlation coefficient for three βs.

Fig. S9. Correlation coefficient analysis of three βs in $\alpha_3\beta_3$ subcomplex observed in AMPPNP. (A) AFM image of $\alpha_3\beta_3$. (B) Reference images and ROIs used in the correlation analysis. Reference images were chosen so that β_1 appears to be in the open state whereas β_2 and β_3 appear to be in the closed state. (C) Correlation coefficient distributions for the three βs. (D) Time courses of correlation coefficient for the three βs.

Fig. S10. Distributions of the number of successive shifts of the "CCO" state in clockwise (top) and counterclockwise (bottom) directions. Distributions at (A) 2 μM, (B) 3 μM, and (C) 4 μM ATP. The direction of the "CCO" shift is clearly biased in the counterclockwise direction. The values for "mean" indicate the average number of successive shifts, and the values for "s.d." indicate the standard deviations.

Fig. S11. Histograms of dwell times for the open (top) and closed (bottom) states in various concentrations of ATP (A: 2 μM, $n = 266$; B: 3 μM, $n = 426$; C: 4 μM, $n = 374$). Dwell time distributions for the open state are well fitted with single exponential decay functions (solid lines on top). The distributions for the closed state are fitted with functions representing consecutive reactions with two identical time constants:
$A \times t \times \exp(-t/\tau)$ (solid lines on bottom).

Fig. S12. Loss of a single subunit stops rotary propagation of conformational changes. (A and D) AFM images before and after loss of β_1 (A) or α_1 (D) (Online movies S7 and S8). (B and E) Time courses of correlation coefficients for the three βs designated in (A) and (D), respectively. Solid horizontal lines show the mean correlation coefficients for the periods of open and closed states. The states are judged by examining whether the correlation coefficients are above or below a threshold (0.978). β_1 (B) is lost at 16.2 s and α_1 (E) is lost at 9.4 s (vertical broken lines). (C and F) Cumulated angles of open β measured using the highest pixel position in each frame. [ATP], 2 μM; frame rate, 12.5 fps.

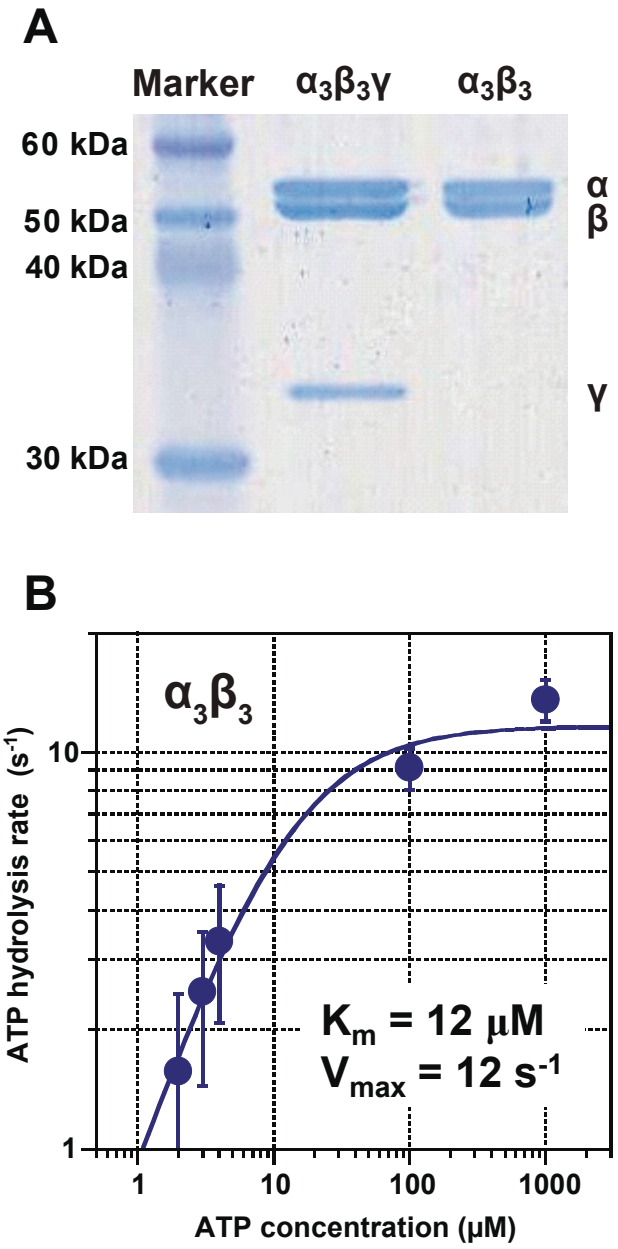
A
Marker
α3β3γ
α3β3
60 kDa
50 kDa
40 kDa
30 kDa
α
β
γ
B
α3β3
ATP hydrolysis rate (s-1)
10
1
Km = 12 μM
Vmax = 12 s-1
1
10
100
1000
ATP concentration (μM)

Fig. S1

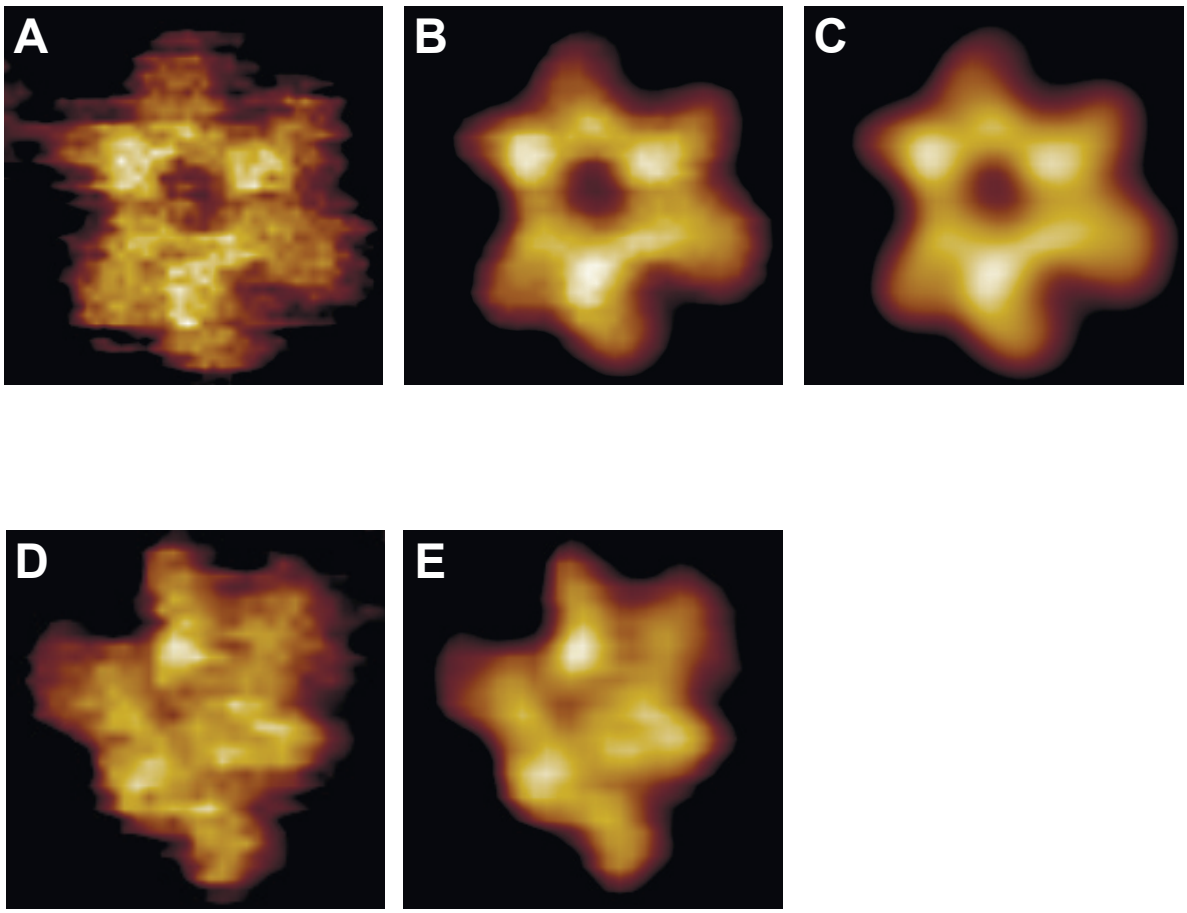

Fig. S2

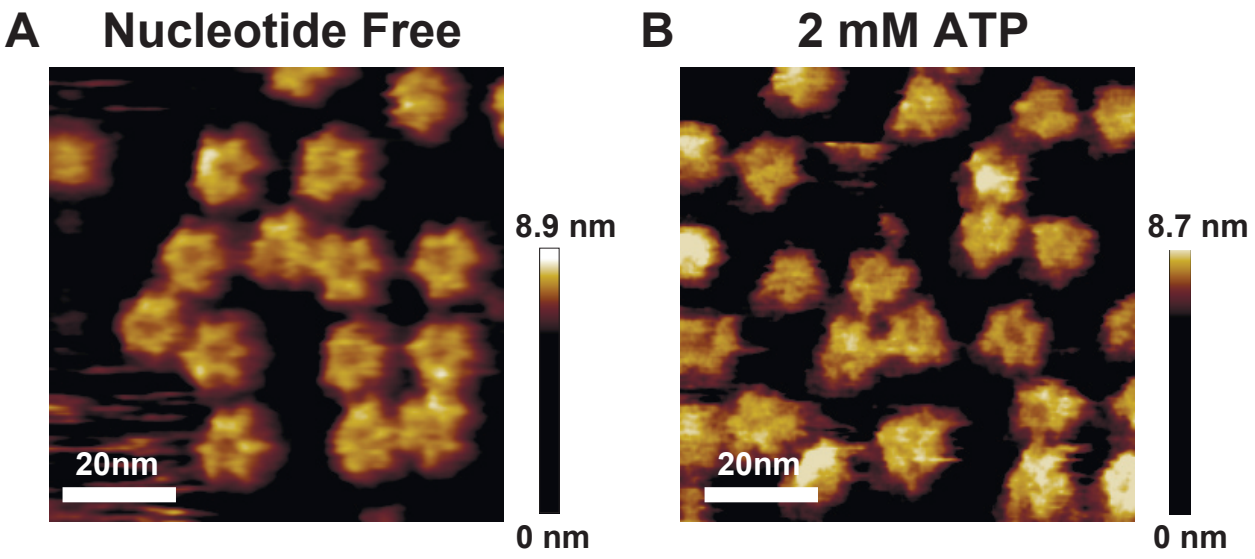

Fig. S3

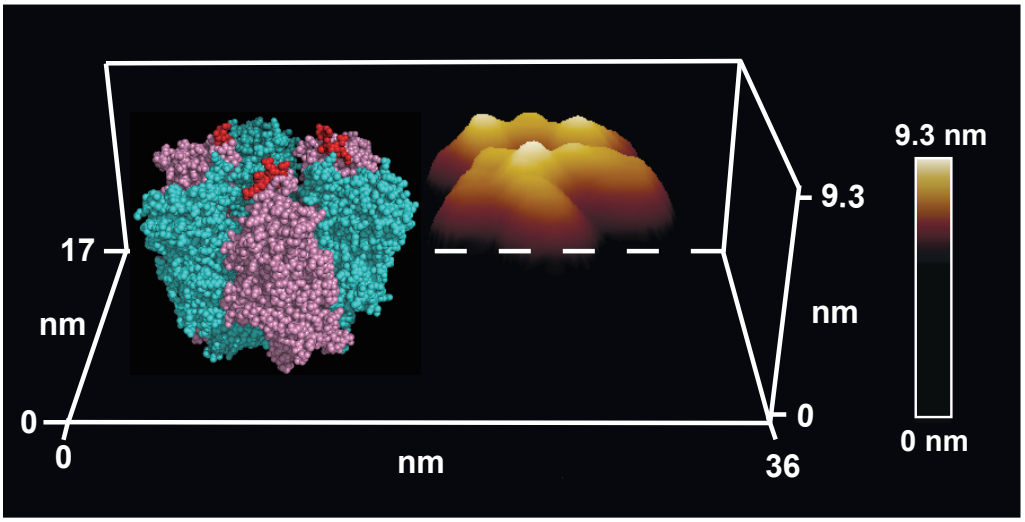

Fig. S4

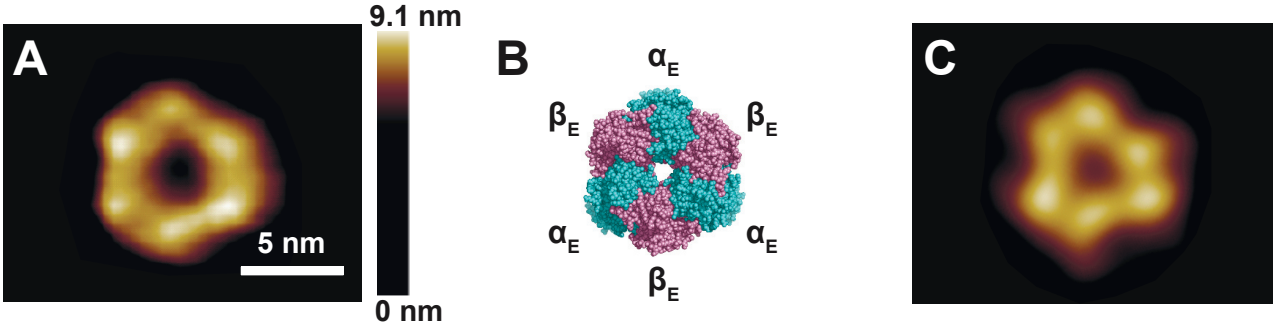

Fig. S5

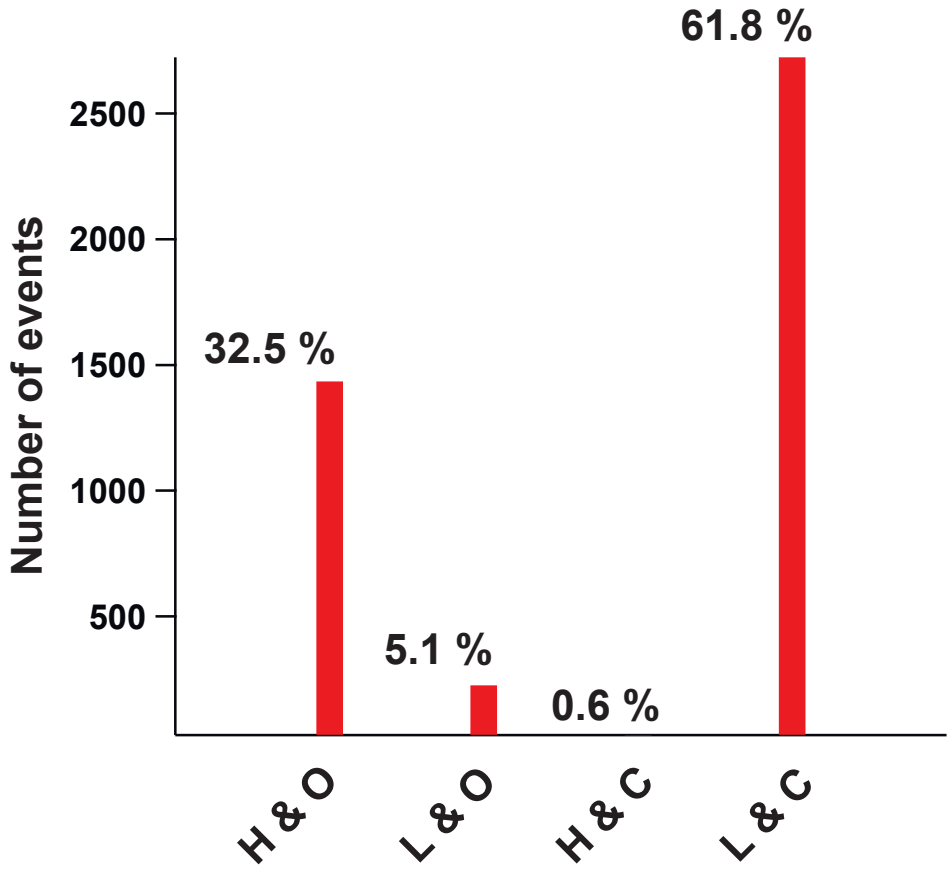
61.8 %
2500
2000
Number of events
1500
32.5 %
1000
500
5.1 %
0.6 %
H&O
L&O
H&C
L&C

Fig. S6

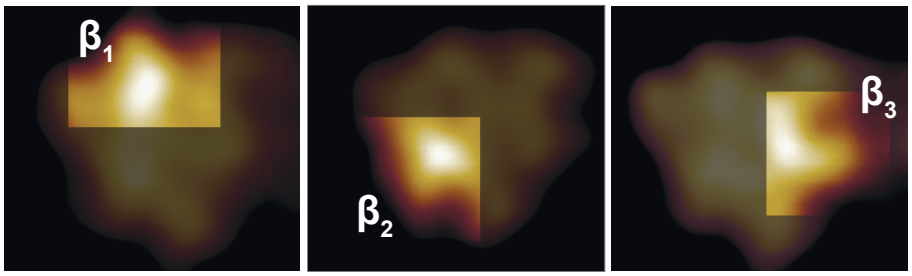

Fig. S7

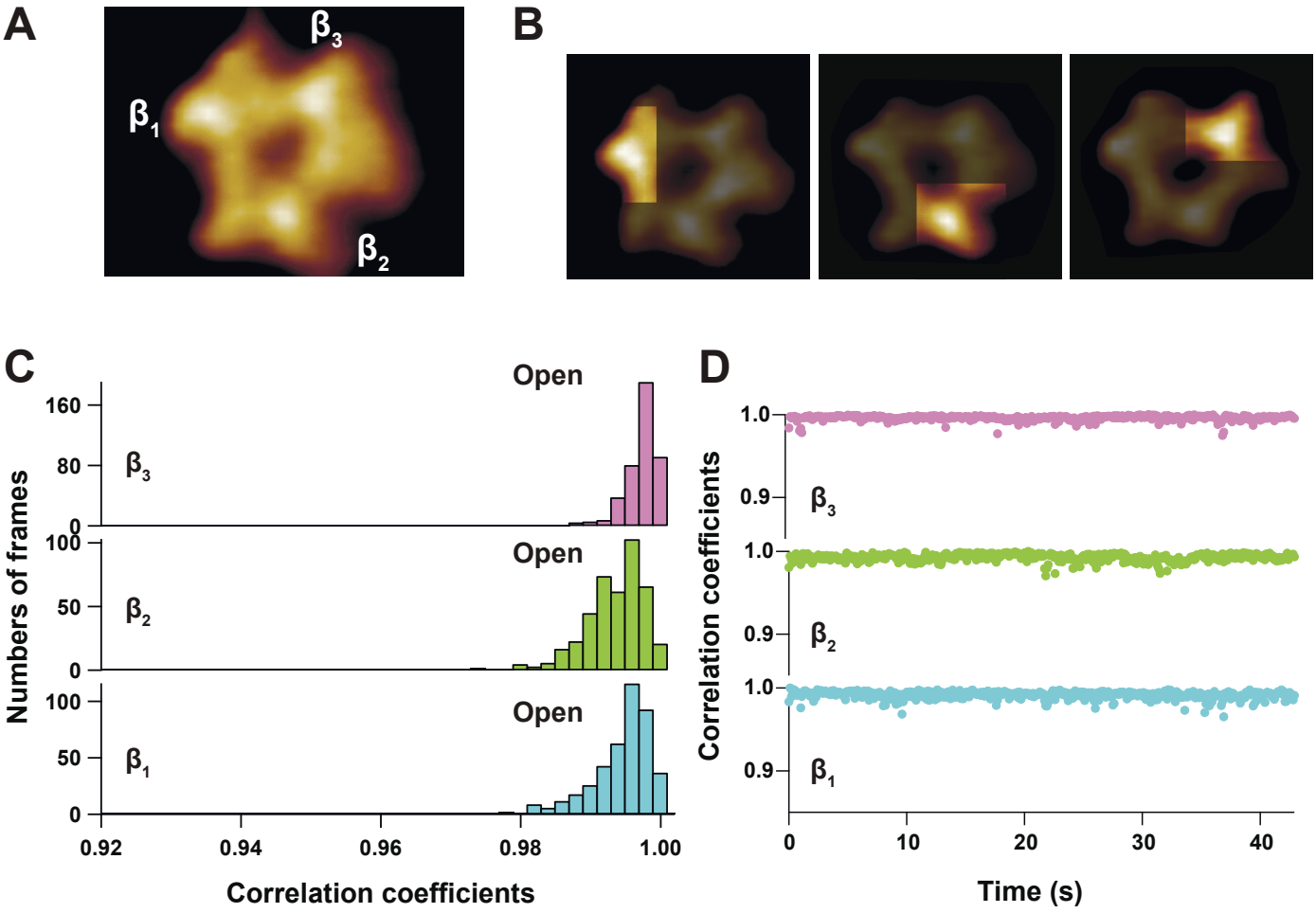
A
β3
β1
β2
B
C
Open
160
80
0
β3
100
50
0
β2
100
50
0
β1
Numbers of frames
0.92
0.94
0.96
0.98
1.00
Correlation coefficients
D
1.0
0.9
β3
β2
β1
Correlation coefficients
0
10
20
30
40
Time (s)

Fig. S8

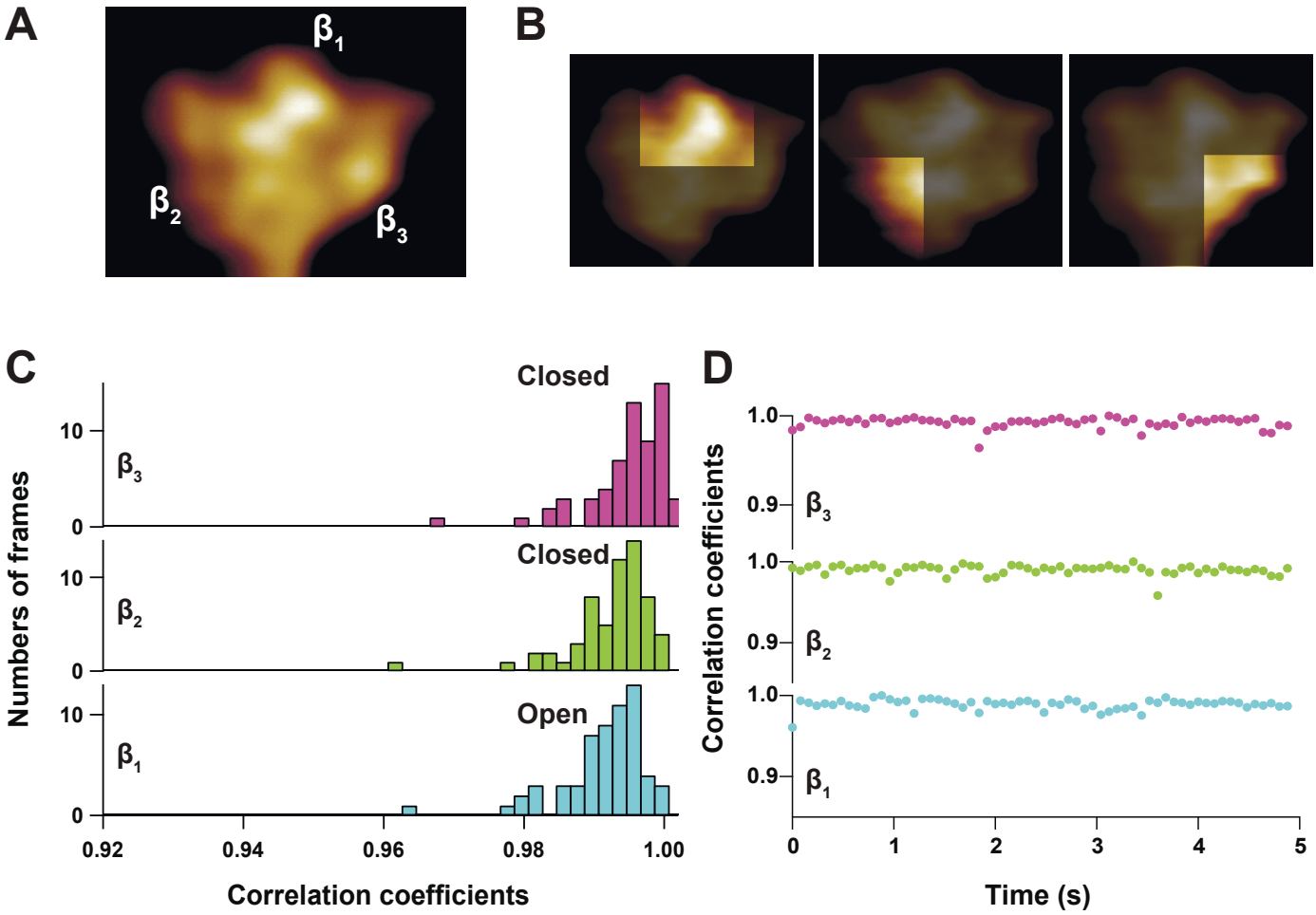
A
β1
β2
β3
B
C
Closed
Closed
Open
β3
β2
β1
10
0
Numbers of frames
0.92
0.94
0.96
0.98
1.00
Correlation coefficients
D
1.0
0.9
Correlation coefficients
0
1
2
3
4
5
Time (s)

Fig. S9

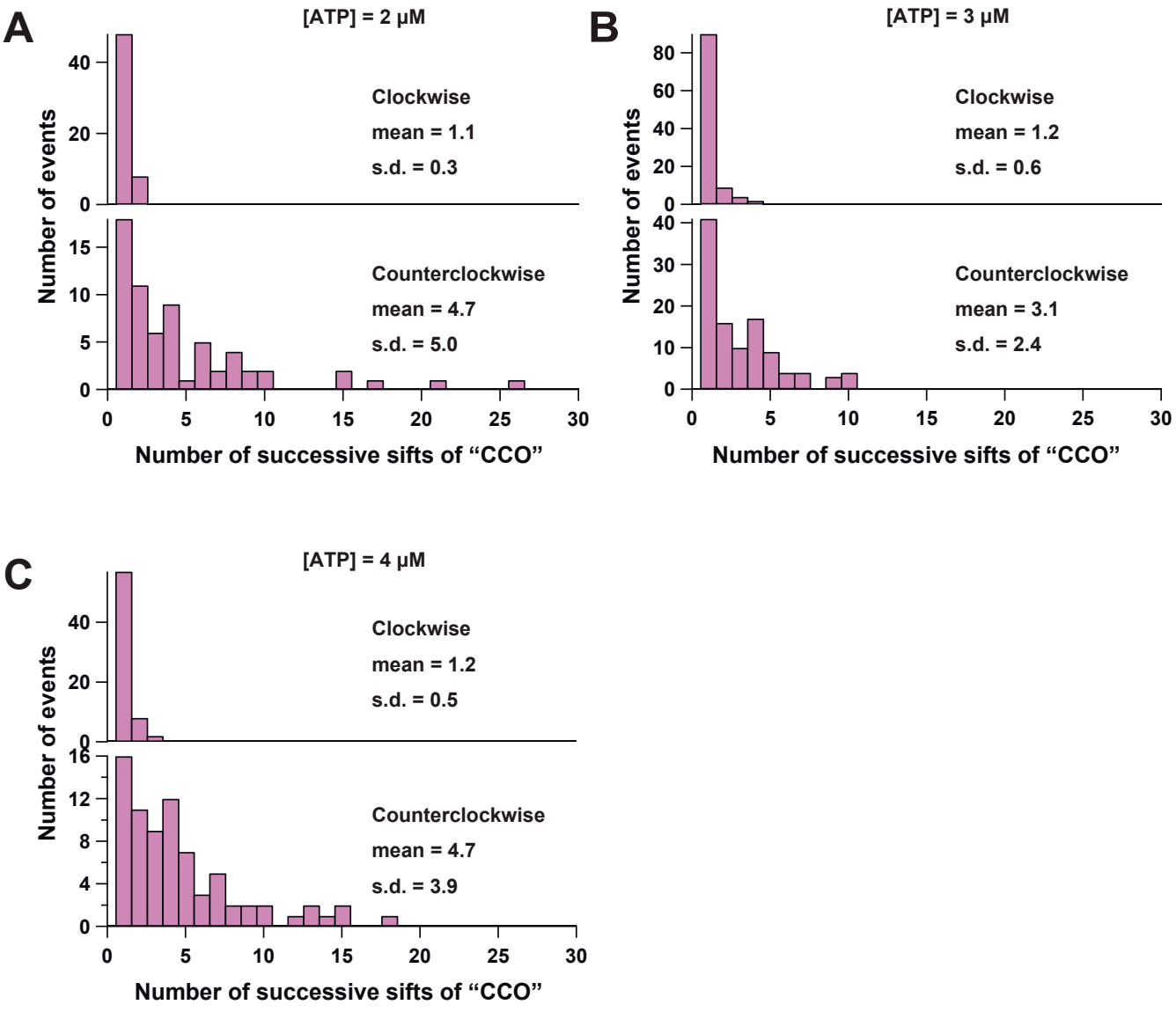
A
[ATP] = 2 μM
Clockwise
mean = 1.1
s.d. = 0.3
Counterclockwise
mean = 4.7
s.d. = 5.0
Number of events
Number of successive sifts of "CCO"
B
[ATP] = 3 μM
Clockwise
mean = 1.2
s.d. = 0.6
Counterclockwise
mean = 3.1
s.d. = 2.4
Number of events
Number of successive sifts of "CCO"
C
[ATP] = 4 μM
Clockwise
mean = 1.2
s.d. = 0.5
Counterclockwise
mean = 4.7
s.d. = 3.9
Number of events
Number of successive sifts of "CCO"

Fig. S10

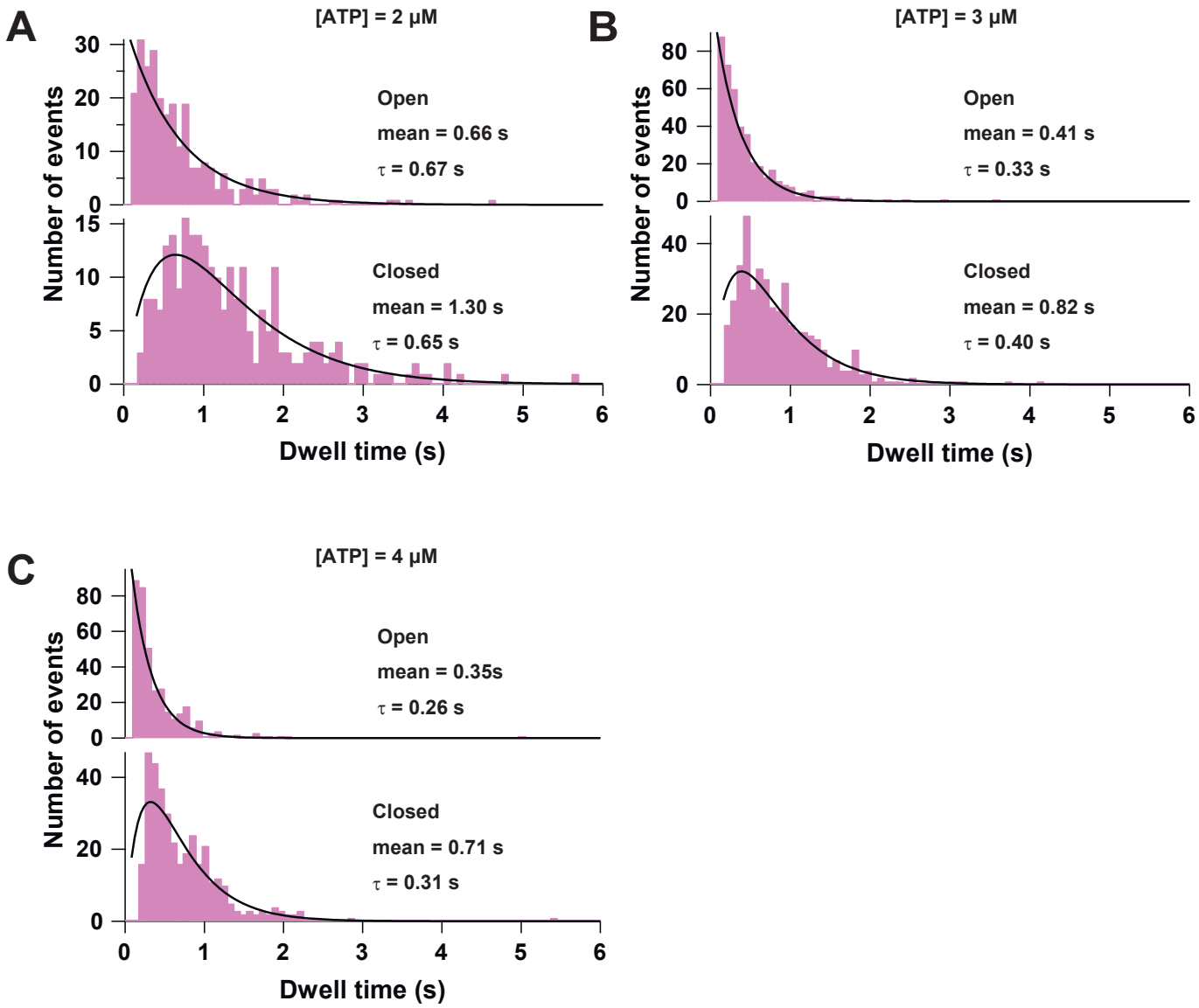
A
[ATP] = 2 μM
Open
mean = 0.66 s
τ = 0.67 s
Closed
mean = 1.30 s
τ = 0.65 s
Number of events
Dwell time (s)
B
[ATP] = 3 μM
Open
mean = 0.41 s
τ = 0.33 s
Closed
mean = 0.82 s
τ = 0.40 s
Number of events
Dwell time (s)
C
[ATP] = 4 μM
Open
mean = 0.35s
τ = 0.26 s
Closed
mean = 0.71 s
τ = 0.31 s
Number of events
Dwell time (s)

Fig. S11

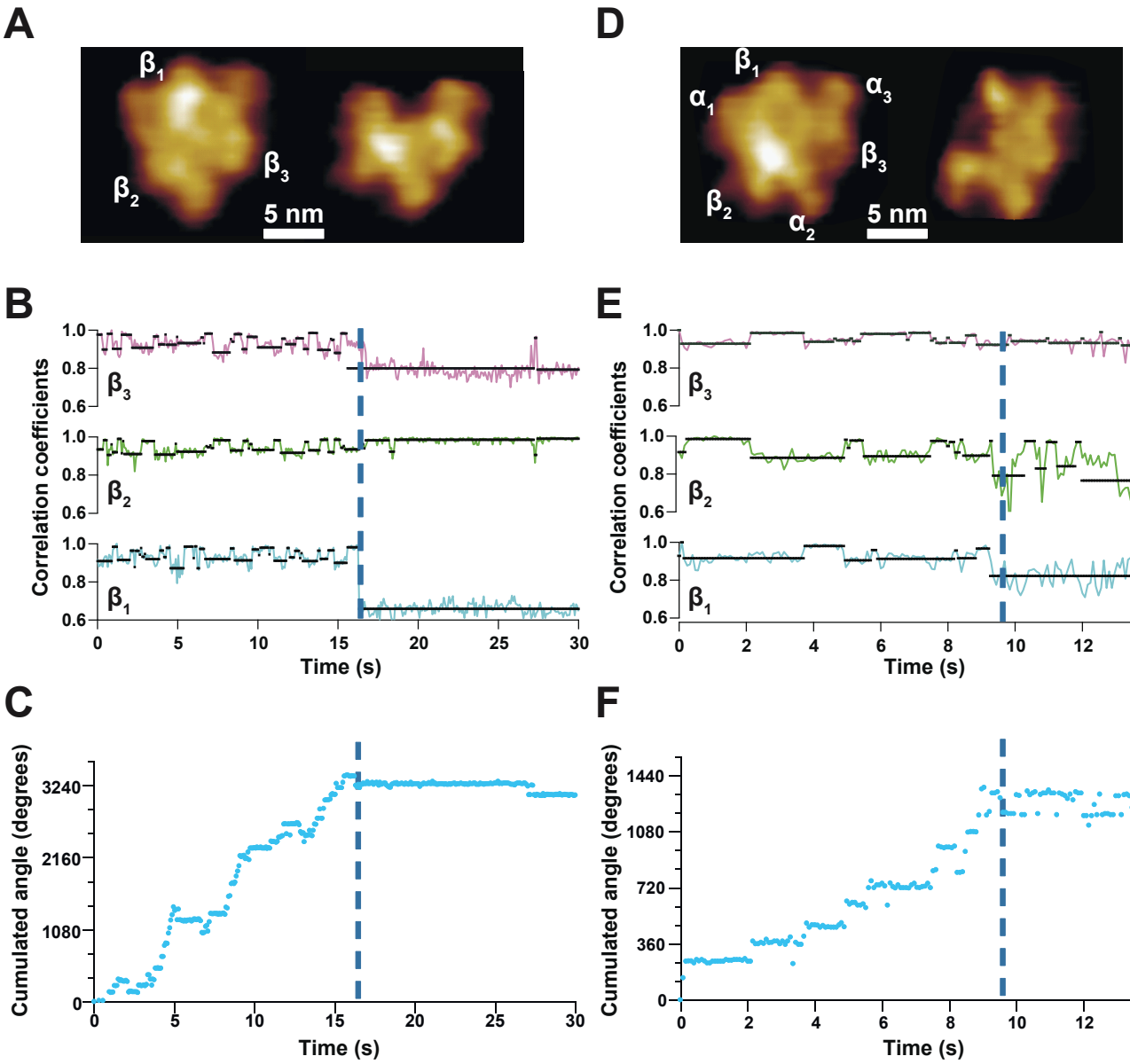
A
β1
β2
β3
5 nm
D
β1
α1
α3
β3
β2
α2
5 nm
B
Correlation coefficients
β3
β2
β1
Time (s)
E
Correlation coefficients
β3
β2
β1
Time (s)
C
Cumulated angle (degrees)
Time (s)
F
Cumulated angle (degrees)
Time (s)

Fig. S12

Table S1. Fraction of molecules showing conformational changes under various nucleotide conditions.

Nucleotide conditions	Number of observed molecules	Number of change-detected molecules	Fraction of change-detected molecules
Nucleotide-free	53	0	0%
1 mM AMPPNP	46	0	0%
2 μM ATP	95	90	89%
3 μM ATP	86	81	94%
4 μM ATP	64	62	97%

References and Notes

1. P. D. Boyer, The ATP synthase—a splendid molecular machine. *Annu. Rev. Biochem.* **66**, 717 (1997). doi:10.1146/annurev.biochem.66.1.717 Medline

2. W. Junge, H. Sielaff, S. Engelbrecht, Torque generation and elastic power transmission in the rotary F_OF_1-ATPase. *Nature* **459**, 364 (2009). doi:10.1038/nature08145 Medline

3. M. J. Gresser, J. A. Myers, P. D. Boyer, Catalytic site cooperativity of beef heart mitochondrial F_1 adenosine triphosphatase. Correlations of initial velocity, bound intermediate, and oxygen exchange measurements with an alternating three-site model. *J. Biol. Chem.* **257**, 12030 (1982). Medline

4. J. P. Abrahams, A. G. Leslie, R. Lutter, J. E. Walker, Structure at 2.8 A resolution of F_1-ATPase from bovine heart mitochondria. *Nature* **370**, 621 (1994). doi:10.1038/370621a0 Medline

5. H. Noji, R. Yasuda, M. Yoshida, K. Kinosita Jr., Direct observation of the rotation of F_1-ATPase. *Nature* **386**, 299 (1997). doi:10.1038/386299a0 Medline

6. H. Wang, G. Oster, Energy transduction in the F_1 motor of ATP synthase. *Nature* **396**, 279 (1998). doi:10.1038/24409 Medline

7. C. Kaibara, T. Matsui, T. Hisabori, M. Yoshida, Structural asymmetry of F_1-ATPase caused by the gamma subunit generates a high affinity nucleotide binding site. *J. Biol. Chem.* **271**, 2433 (1996). doi:10.1074/jbc.271.5.2433 Medline

8. J. J. García, R. A. Capaldi, Unisite catalysis without rotation of the γ-ε domain in *Escherichia coli* F_1-ATPase. *J. Biol. Chem.* **273**, 15940 (1998). doi:10.1074/jbc.273.26.15940 Medline

9. R. K. Nakamoto, C. J. Ketchum, M. K. al-Shawi, Rotational coupling in the F_0F_1 ATP synthase. *Annu. Rev. Biophys. Biomol. Struct.* **28**, 205 (1999). doi:10.1146/annurev.biophys.28.1.205 Medline

10. H. Itoh *et al*., Mechanically driven ATP synthesis by F1-ATPase. *Nature* **427**, 465 (2004). doi:10.1038/nature02212 Medline

11. Y. Rondelez *et al*., Highly coupled ATP synthesis by F_1-ATPase single molecules. *Nature* **433**, 773 (2005). doi:10.1038/nature03277 Medline

12. Y. Iko, K. V. Tabata, S. Sakakihara, T. Nakashima, H. Noji, Acceleration of the ATP-binding rate of F_1-ATPase by forcible forward rotation. *FEBS Lett.* **583**, 3187 (2009). doi:10.1016/j.febslet.2009.08.042 Medline

13. S. Furuike *et al*., Axle-less F_1-ATPase rotates in the correct direction. *Science* **319**, 955 (2008). doi:10.1126/science.1151343 Medline

14. N. Mnatsakanyan, A. M. Krishnakumar, T. Suzuki, J. Weber, The role of the βDELSEED-loop of ATP synthase. *J. Biol. Chem.* **284**, 11336 (2009). doi:10.1074/jbc.M900374200 Medline
15. M. Yoshida, W. S. Allison, The ATPase activity of the alpha 3 beta 3 complex of the F_1-ATPase of the thermophilic bacterium PS3 is inactivated on modification of tyrosine 307 in a single beta subunit by 7-chloro-4-nitrobenzofurazan. *J. Biol. Chem.* **265**, 2483 (1990). Medline
16. P. Aloise, Y. Kagawa, P. S. Coleman, Comparative Mg(2+)-dependent sequential covalent binding stoichiometries of 3′-O-(4-benzoyl)benzoyl adenosine 5′-diphosphate of MF1, TF1, and the alpha 3 beta 3 core complex of TF1. The binding change motif is independent of the F1 gamma delta epsilon subunits. *J. Biol. Chem.* **266**, 10368 (1991). Medline
17. T. Ando *et al*., A high-speed atomic force microscope for studying biological macromolecules. *Proc. Natl. Acad. Sci. U.S.A.* **98**, 12468 (2001). doi:10.1073/pnas.211400898 Medline
18. T. Ando, T. Uchihashi, T. Fukuma, High-speed atomic force microscopy for nano-visualization of dynamic biomolecular processes. *Prog. Surf. Sci.* **83**, 337 (2008). doi:10.1016/j.progsurf.2008.09.001
19. M. Shibata, H. Yamashita, T. Uchihashi, H. Kandori, T. Ando, High-speed atomic force microscopy shows dynamic molecular processes in photoactivated bacteriorhodopsin. *Nat. Nanotechnol.* **5**, 208 (2010). doi:10.1038/nnano.2010.7 Medline
20. N. Kodera, D. Yamamoto, R. Ishikawa, T. Ando, Video imaging of walking myosin V by high-speed atomic force microscopy. *Nature* **468**, 72 (2010). doi:10.1038/nature09450 Medline
21. Y. Shirakihara *et al*., The crystal structure of the nucleotide-free alpha 3 beta 3 subcomplex of F_1-ATPase from the thermophilic Bacillus PS3 is a symmetric trimer. *Structure* **5**, 825 (1997). doi:10.1016/S0969-2126(97)00236-0 Medline
22. R. I. Menz, J. E. Walker, A. G. Leslie, Structure of bovine mitochondrial F_1-ATPase with nucleotide bound to all three catalytic sites: Implications for the mechanism of rotary catalysis. *Cell* **106**, 331 (2001). doi:10.1016/S0092-8674(01)00452-4 Medline
23. K. Adachi *et al*., Coupling of rotation and catalysis in F_1-ATPase revealed by single-molecule imaging and manipulation. *Cell* **130**, 309 (2007). doi:10.1016/j.cell.2007.05.020 Medline
24. R. Watanabe, R. Iino, H. Noji, Phosphate release in F_1-ATPase catalytic cycle follows ADP release. *Nat. Chem. Biol.* **6**, 814 (2010). doi:10.1038/nchembio.443 Medline

25. E. J. Enemark, L. Joshua-Tor, On helicases and other motor proteins. *Curr. Opin. Struct. Biol.* **18**, 243 (2008). doi:10.1016/j.sbi.2008.01.007 Medline
26. S. Sakakihara, S. Araki, R. Iino, H. Noji, A single-molecule enzymatic assay in a directly accessible femtoliter droplet array. *Lab Chip* **10**, 3355 (2010). doi:10.1039/c0lc00062k Medline
27. T. R. Rodríguez, R. Garcia, Theory of Q control in atomic force microscopy. *Appl. Phys. Lett.* **82**, 4821 (2003). doi:10.1063/1.1584790
28. M. Wendel, H. Lorenz, J. P. Kotthaus, Sharpened electron beam deposited tips for high resolution atomic force microscope lithography and imaging. *Appl. Phys. Lett.* **67**, 3732 (1995). doi:10.1063/1.115365